Remote sensing of surface energy fluxes at 10^1-m pixel resolutions

J. M. Norman,[1] M. C. Anderson,[1] W. P. Kustas,[2] A. N. French,[2,3] J. Mecikalski,[4] R. Torn,[1,5] G. R. Diak,[4] T. J. Schmugge,[2] and B. C. W. Tanner[1,6]

Received 16 October 2002; revised 18 March 2003; accepted 7 May 2003; published 28 August 2003.

[1] Many applications exist within the fields of agriculture, forestry, land management, and hydrologic assessment for routine estimation of surface energy fluxes, particularly evapotranspiration (ET), at spatial resolutions of the order of 10^1 m. A new two-step approach (called the disaggregated atmosphere land exchange inverse model, or DisALEXI) has been developed to combine low- and high-resolution remote sensing data to estimate ET on the 10^1–10^2 m scale without requiring any local observations. The first step uses surface brightness-temperature-change measurements made over a 4-hour morning interval from the GOES satellite to estimate average surface fluxes on the scale of about 5 km with an algorithm known as ALEXI. The second step disaggregates the GOES 5-km surface flux estimates by using high-spatial-resolution images of vegetation index and surface temperature, such as from ASTER, Landsat, MODIS, or aircraft, to produce high-spatial-resolution maps of surface fluxes. Using data from the Southern Great Plains field experiment of 1997, the root-mean-square difference between remote estimates of surface fluxes and ground-based measurements is about 40 W m^{-2}, comparable to uncertainties associated with micrometeorological surface flux measurement techniques. The DisALEXI approach was useful for estimating field-scale, surface energy fluxes in a heterogeneous area of central Oklahoma without using any local observations, thus providing a means for scaling kilometer-scale flux estimates down to a surface flux-tower footprint. Although the DisALEXI approach is promising for general applicability, further tests with varying surface conditions are necessary to establish greater confidence. *INDEX TERMS:* 3360 Meteorology and Atmospheric Dynamics: Remote sensing; 3322 Meteorology and Atmospheric Dynamics: Land/atmosphere interactions; 1818 Hydrology: Evapotranspiration; 3337 Meteorology and Atmospheric Dynamics: Numerical modeling and data assimilation; *KEYWORDS:* thermal infrared, remote sensing, disaggregation, surface flux models

Citation: Norman, J. M., M. C. Anderson, W. P. Kustas, A. N. French, J. Mecikalski, R. Torn, G. R. Diak, T. J. Schmugge, and B. C. W. Tanner, Remote sensing of surface energy fluxes at 10^1-m pixel resolutions, *Water Resour. Res.*, *39*(8), 1221, doi:10.1029/2002WR001775, 2003.

1. Introduction

[2] The partitioning of net radiation at a land surface into latent and sensible heat fluxes reflects the physical characteristics of the surface: its roughness, moisture content, vegetation cover, and so forth. Surface flux partitioning also influences the coupling between the surface and the lower atmosphere. Whether one is interested in studying the influence of surface fluxes on the lower atmosphere or in characterizing the nature of the surface itself, much can be learned by quantifying the temporal and spatial character of the surface energy balance using remotely sensed data. There is particular demand for operational methodologies for mapping surface fluxes, algorithms that can be executed remotely and routinely and do not require any local, ground-based data as input.

[3] Numerous applications exist for operational maps of energy balance/evapotranspiration (ET) made at a broad range in spatial scales. The routine estimation of surface fluxes at regional scales (i.e., ~10–100 km), for example, would benefit numerical weather forecasting in terms of defining accurate model boundary conditions. At high spatial resolution (i.e., 10^1 m), remote estimates of ET provide a means to calibrate models simulating site-specific energy and water balances of agricultural crops, which use transpiration-rate estimates to detect productivity-limiting field conditions and project end-of-season yields [*Moran et al.*, 1995; *Moulin et al.*, 1998]. In forested areas, the transpiration rate is also the primary indicator of forest health and vulnerability to fire [*Vidal and Devaux-Ros*, 1995]. Changes in the energy balance are indicative of changes in cropland and natural ecosystem functioning; hence remote sensing models have potential in mapping and monitoring plant ecosystem health [*Moran*, 2003]. At

[1]Department of Soil Science, University of Wisconsin, Madison, Wisconsin, USA.
[2]USDA-ARS, Hydrology and Remote Sensing Lab, Beltsville, Maryland, USA.
[3]Now at Hydrological Sciences Branch, NASA Space Flight Center, Greenbelt, Maryland, USA.
[4]Space Science and Engineering Center, University of Wisconsin, Madison, Wisconsin, USA.
[5]Now at Department of Atmospheric Science, University of Washington, Seattle, Washington, USA.
[6]Now at Biomedical Engineering, University of Washington, Seattle, Washington, USA.

0043-1397/03/2002WR001775$09.00

these scales, maps of daily ET can also be used to constrain recharge in detailed transient hydrologic models.

[4] Unfortunately, methodologies using high-resolution remotely sensed data with 10^1-10^2 m pixel resolution generally rely on the availability of contemporaneous in situ measurements, primarily near-surface meteorological conditions such as air temperature, wind speed, and humidity, and are therefore difficult to implement operationally [*Gardner et al.*, 1992; *Choudhury et al.*, 1994; *Moran et al.*, 1994; *Moran et al.*, 1996]. Routine application of high-resolution satellite data is also hindered by the long return period between successive satellite overpasses. The frequency of repeated coverage from the Land Remote-Sensing Satellite (Landsat) or the Advanced Spaceborne Thermal Emission Reflectance Radiometer (ASTER), for example, is typically of the order of several weeks. Considering that cloud cover will obscure some fraction of these images, monthly coverage is a reasonable expectation for the availability of high-resolution satellite images. Using one snapshot of the surface per month for estimating spatially distributed surface heat fluxes and evapotranspiration (ET) severely limits the utility for operational monitoring of vegetation conditions [*Moran et al.*, 1996].

[5] For coarser resolutions of 10^3-10^4 m, satellite coverage is much more frequent, and hence surface fluxes have been estimated with data from satellites such as the Geostationary Operational Environmental Satellite (GOES), Meteosat, or the Advanced Very High Resolution Radiometer (AVHRR). On these spatial scales, the need for ancillary meteorological data can be reduced by coupling land-surface models with atmospheric models [e.g., *Carlson*, 1986; *Taconet et al.*, 1986; *Price*, 1990; *Seguin et al.*, 1991; *Mecikalski et al.*, 1999]. However, validation of such coarse-scale flux models has been problematic due to limitations related to the network of available flux observations and the scale mismatch between the resolution of model output and the in situ flux measurement footprint.

[6] To date, the validation of coarse-scale remote-sensing methods for estimating surface fluxes has rested on three strategies: (1) using ground- or tower-based measurements of inputs to, and outputs from, algorithms that will ultimately be used on the kilometer spatial scale, (2) direct comparison of ground-based micrometeorological surface flux measurements (representative of a 10^2-m scale footprint) with model estimates using satellite data having pixel resolutions of 1–5 km, or (3) by direct comparison to low-altitude aircraft flux measurements. The first strategy [e.g., *Moran et al.*, 1994; *Friedl*, 1996; *Zhan et al.*, 1996; *Anderson et al.*, 1997; *Gillies et al.*, 1997; *Norman et al.*, 2000] may be most efficient for the initial validation of a new approach, but it is not a true test of the algorithm's utility at the larger scale and ignores the practical issues involved in gathering operational inputs remotely. The second strategy assumes the surface flux measurement to be representative of the entire satellite 1–5 km pixel scene [*Gao et al.*, 1998; *Mecikalski et al.*, 1999; *Song et al.*, 2000; *Jiang and Islam*, 2001], requiring homogeneity at the scale of several satellite pixels considering registration uncertainties. A look at almost any Landsat scene will reveal that homogeneous land-surface patches on the scale of several kilometers are exceedingly rare in most places. Predicted surface fluxes from the First ISLSCP Field Experiment (FIFE), for example, showed a dominant spatial scale of 100–200 m [*Divakarla*, 1997]. The third approach [*Song et al.*, 2000; *Kustas et al.*, 2001] has been used successfully but with mixed results because of limitations associated with flying at 50-m altitudes and challenges in interpreting boundary-layer phenomena [*Mahrt*, 1998].

[7] This study reports on a flux disaggregation methodology designed to bridge the gap in spatial resolution between ground-based micrometeorological measurements of surface fluxes (100-m scale) and coarse-scale (10^3 m) remote-sensing observations. The scheme uses a coupled land-surface atmospheric-boundary-layer model referred to as the ALEXI (Atmosphere Land Exchange Inverse) model, which has been shown to be very robust in estimating large-scale surface fluxes while requiring no in situ information [*Anderson et al.*, 1997; *Mecikalski et al.*, 1999]. The scaling assumptions embedded in this disaggregation technique are similar to those in the "mosaic" or "tile" approach of *Koster and Suarez* [1992], which are supported by observational and theoretical studies for surfaces having length scales of heterogeneity of the order of 10^2-10^3 m [*Claussen*, 1995; *Mahrt*, 1996; *Kustas et al.*, 1999].

[8] The disaggregation approach we describe here combines the high-temporal, low-spatial resolution of GOES with the low-temporal, high-spatial resolution of aircraft-based remotely sensed data collected during the 1997 Southern Great Plains (SGP97) Experiment conducted in Oklahoma [*Jackson et al.*, 1999]. The resulting multiscale data set is used to estimate surface fluxes over a 5×5 km GOES pixel at 24-m pixel resolution without the need for any additional ground-based input. The high-resolution surface heat flux predictions are reaggregated using a weighted flux footprint analysis and compared to micrometeorological flux measurements and to flux estimates using in situ meteorological observations.

2. Approach

2.1. The Disaggregation Algorithm

[9] The disaggregation algorithm developed here draws on the concept of the "blending height," the height where wind speed and scalars can be treated as uniform over the landscape [*Wierenga*, 1986; *Mason*, 1988]. *Blyth* [1995] showed how the blending height principle can be modeled simply for a mixture of two surfaces, although its application to an agricultural patchwork of surfaces is not readily apparent. Fortunately, under a wide range of surface conditions the blending height can be taken to be at the top of the surface layer, which is of the order of 50 m [*Raupach and Finnigan*, 1995].

[10] Here the air temperature at the blending height is estimated with the regional-scale ALEXI model (Figure 1). At the core of ALEXI is a two-source surface flux model (TSM) [*Norman et al.*, 1995b; *Kustas and Norman*, 1999] (a brief description is also presented in Appendix A) which deconvolves the composite radiometric surface temperature $T_{RAD}(\phi)$ observed at view angle ϕ into soil and canopy contributions given an estimate of the vegetation cover fraction within the scene (f_c). The lower boundary conditions for the two-source model are provided by remote thermal infrared observations taken at two times during the

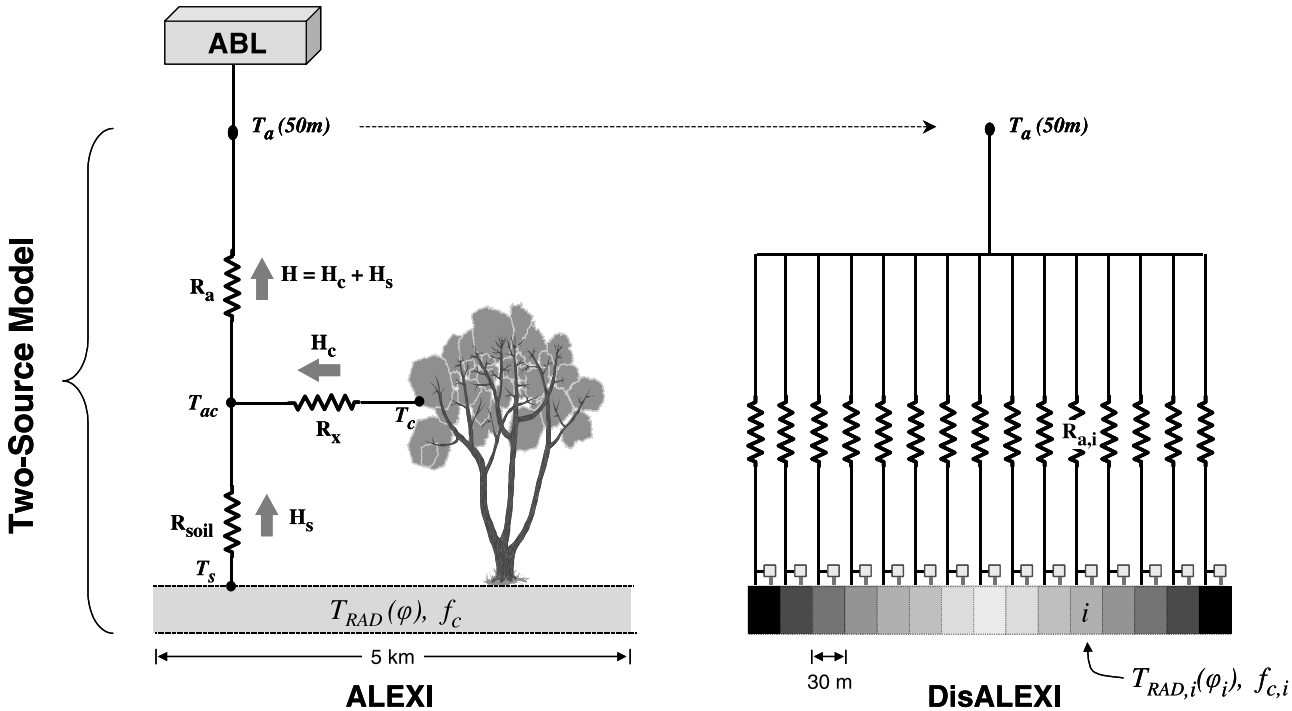

Figure 1. Schematic diagram representing the coupled ALEXI/DisALEXI modeling scheme.

morning hours (about 1.5 and 5.5 hours past sunrise) with a geostationary satellite such as GOES, nominally at 4–5 km spatial resolution. The amplitude oFFf the diurnal temperature curve is related to surface moisture content and therefore is an indicator of surface flux partitioning [*Price*, 1980; *Carlson et al.*, 1981]. Furthermore, use of a time differential measurement reduces the effects of errors in sensor calibration and surface emissivity specification.

[11] Closure for the system energy budget is obtained using a simple one-dimensional slab model of atmospheric boundary layer (ABL) development [*McNaughton and Spriggs*, 1986], which relates the morning rise in air temperature above the canopy and the growth in height in the boundary layer to the time-integrated influx of sensible heating from the surface (see Appendix A for further details). The air temperature at the blending height (T_a in equations (A10) and (A18) and θ_m in equation (A17)) is diagnosed at the interface between the surface and boundary layer models and is consistent with the cover fraction and surface temperature change associated with the 5-km patch of landscape contained within the GOES pixel and with the overlying boundary-layer dynamics.

[12] ALEXI works most appropriately at the 5–10 km scale, approximately the scale at which atmospheric forcing from organized surface behavior becomes effective as far as the structure of the ABL is concerned. Vegetation cover fraction and surface temperature can, however, be sampled at much higher resolution, for example, using data from aircraft, Landsat, ASTER, or the Moderate-Resolution Imaging Spectroradiometer (MODIS). In the second phase of the disaggregation process (referred to as DisALEXI), the TSM is applied again, this time to high-resolution images of surface cover ($f_{c,i}$) and surface radiometric temperature ($T_{RAD,i}(\phi_i)$). Here the subscript i, where $i = 1$ to N, refers to the set of N high-resolution pixels contained within one GOES pixel. For this second, fine-scale application of the TSM, the air temperature at 50 m is held constant over the entire 5-km GOES pixel area at the value determined by ALEXI (T_a; see Figure 1). In this hybrid mode, the ABL component of ALEXI is used at the large scales it is best suited for, while the surface component can be applied at much finer scales.

[13] Sensitivity studies with ALEXI have shown that the air temperature calculated at the blending height adjusts to instrumental biases in the surface radiometric temperature measurement, preserving the relationship between the observed temporal change in surface temperature and modeled heat flux ABL evolution [*Anderson et al.*, 1997]. In general, this computed temperature will be preferable to an actual measurement of air temperature made aloft, unless the surface and air temperature observations are well matched in time and their relative uncertainty is much less than a degree. Just a 1°C error in the assumed surface-to-air temperature gradient can translate into errors in predicted sensible heating of up to 100 W m^{-2}, depending on wind speed and surface roughness [*Norman et al.*, 1995a]. In general, air temperature measurements at sufficient height and spatial/temporal resolution to drive regional applications of ALEXI are not routinely available. To ensure the ALEXI-derived vertical temperature gradient is preserved in the disaggregation stage, the high-resolution radiometric temperature field is bias corrected to yield an average consistent with the 5-km GOES temperature (see below).

2.2. DisALEXI Input Requirements

[14] *Mecikalski et al.* [1999] review data inputs required for regional-scale application of the ALEXI model. Details regarding specification and processing of input data used in the DisALEXI flux disaggregation process are outlined here.

[15] Four forcing variables are held constant over the 5-km disaggregation domain: the 50-m air temperature and wind speed, and downwelling short- and long-wave radiation. Again, the blending height air temperature is computed by ALEXI; the other three variables are assigned the values input to ALEXI.

[16] All land-surface-related input fields are developed on a grid coincident with the high-resolution radiometric temperature and vegetation cover data and will be designated with the subscript i, as described above, signifying the ith pixel in this grid. Vegetation height is scaled between seasonal minimum and maximum limits (assigned by land-cover class), based on the current vegetation cover fraction in each pixel. This vegetation height is used to estimate the effective aerodynamic roughness of the canopy [*Massman*, 1997] for each pixel and (with appropriate local diabatic corrections) the aerodynamic resistance to vertical transport ($R_{a,i}$; see Figure 1). Net radiation ($R_{n,i}$) is computed with equations from ALEXI (equations (A7)–(A9) in Appendix A), using high-resolution surface temperature information ($T_{RAD,i}(\phi_i)$) and known relationships for surface albedo (A_i) [*Campbell and Norman*, 1998] and surface emissivity (ε_i) [*Anton and Ross*, 1987] as a function of vegetative cover ($f_{c,i}$). Because bare soil and dense vegetation albedos are similar in this study and at many locations, high-resolution pixel to pixel albedo differences affect the available energy by less than 5% if they are ignored. Here, however, cover-dependent adjustments have been made. The fraction of vegetative cover that is green ($f_{g,i}$) is unity for this study; a method for estimating this quantity remotely is discussed by *Kustas and Norman* [1999].

[17] A key step in applying DisALEXI is accommodating likely differences in sensor calibration, atmospheric correction, and view angle between the 5-km GOES surface temperature estimate, $T_{RAD}(\phi)$, and the high-resolution surface temperature observations, $T_{RAD,i}(\phi_i)$. As discussed above, an uncorrected bias between the high-resolution surface temperature data and the blending height air temperature computed by ALEXI will introduce errors into the disaggregated sensible heat flux estimates.

[18] The first step is to adjust all images for atmospheric [*Berk et al.*, 1998] and surface emissivity [*Kustas and Norman*, 1999] effects. Next, using the soil and canopy temperature estimates from ALEXI, the 5-km radiometric temperature from GOES at view angle ϕ is adjusted to the average angle $\bar{\phi}_i$ at which the high-resolution sensor views the scene, using equations (A1) and (A3). This angle-adjusted 5-km temperature, $T_{RAD}(\bar{\phi}_i)$, is used in step three to compute bias-corrected, high-resolution radiometric temperatures ($T^C_{RAD,i}(\phi_i)$) for all N pixels over the GOES pixel as follows:

$$T^C_{RAD,i}(\phi_i) = T_{RAD,i}(\phi_i) + T_{RAD}(\bar{\phi}_i) - \sum_{i=1}^{N} T_{RAD,i}(\phi_i)/N$$

[19] A more rigorous correction would involve adjusting each pixel in the high-resolution scene (each at a slightly different viewing angle) to the GOES view angle and comparing the scene average of this field to the unadjusted GOES temperature $T_{RAD}(\phi)$. This adjustment must be done iteratively, since it requires that disaggregated fields of soil and canopy temperature ($T_{s,i}$ and $T_{c,i}$, respectively) already be available. For the study area considered here, the two techniques yielded negligibly different corrections.

2.3. Disaggregation Procedure

[20] In summary, the DisALEXI algorithm is implemented as follows:

[21] 1. The ALEXI model is run over a large domain using two morning GOES observations at 5-km resolution and ancillary data from a synoptic weather-observing network objectively analyzed to the model grid. The ancillary data include rawinsoundings of the lower atmosphere and the standard World Meteorological Organization (WMO) 10-m wind speed observations scaled to the ALEXI blending height (50 m), providing an estimate of the aerodynamic resistance (R_a) between the surface and 50 m (see Figure 1). The GOES surface temperatures used in ALEXI are atmospherically corrected using MODTRAN [*Berk et al.*, 1998], assuming a surface emissivity of 0.98. Vegetation cover is estimated using the AVHRR normalized-difference vegetation index (NDVI) product, following the method of *Choudhury et al.* [1994].

[22] 2. A high-resolution radiometric surface temperature image, acquired around the time of the second GOES observation (~1030 local standard time), is corrected for atmospheric and surface emissivity effects. The pixels in this high-resolution image of surface radiometric temperature are "matched" to the coincident GOES 5-km pixel by making an offset adjustment to accommodate differences due to different sensor view angles, uncertainties in sensor calibration, and atmospheric correction (as described above).

[23] 3. A high-resolution, multiband visible/near-infrared image is used to create a map of NDVI for the target domain, and this map is converted to vegetative cover using the method of *Choudhury et al.* [1994]. A land cover classification map, constructed from multiband data at comparable resolution, is used in conjunction with the cover map to define various surface properties such as roughness length, displacement height, and albedo.

[24] 4. Net radiation is calculated for each high-resolution pixel using a clear-sky solar radiation calculation, albedo, surface thermal emission from surface radiometric temperature matched to GOES, and sky emission from the *Brutsaert* [1975] equation (see equations (A7)–(A9)).

[25] The two-source model [*Norman et al.*, 1995b; *Kustas and Norman*, 1999] is run on each high-resolution pixel using the 50-m above ground level (agl) air temperature predicted by the ALEXI model (step 1) as an upper boundary condition. This produces high-resolution maps of soil heat conduction, sensible heat, and latent heat flux.

[26] The DisALEXI flux estimates are validated by comparison with in situ eddy-covariance measurements using the simple analytical flux-footprint analysis of *Schuepp et al.* [1990] for estimating the relative source-area contributions of multiple high-resolution pixels upwind of the measurement tower.

3. Materials and Methods

[27] The DisALEXI algorithm has been tested with data collected during the Southern Great Plains Experiment of 1997 (SGP97), conducted during June and July in the state of Oklahoma. Details concerning SGP97 are given by

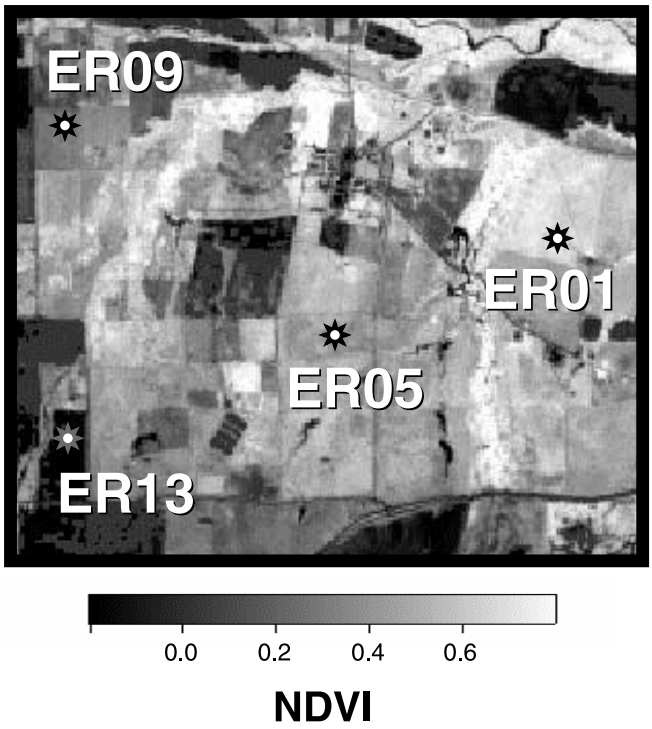

Figure 2. Location of eddy-covariance flux towers within the El Reno, Oklahoma, study area, overlaid on a map of NDVI generated from TMS visible/NIR images acquired on DOY 183.

Jackson et al. [1999], with further description available on the World Wide Web (http://hydrolab.arsusda.gov/sgp97/). Land use in this part of the Great Plains is primarily winter wheat fields and grasslands used for grazing cattle. The aircraft and surface flux data used in this study come from one of three experimental sites that were intensively monitored during SGP97: the USDA-ARS Grazing Lands research facility near El Reno, Oklahoma.

3.1. Ground-Based Observations

[28] The ground-based data used here for validation were acquired at four eddy-covariance towers operating within the El Reno study area (see Figure 2). These tower sites consist of two native grassland or rangeland areas, a pasture site under agricultural management, and a harvested winter wheat field recently tilled and converted to bare soil. The average vegetation height in the rangeland sites was ~0.5 m, and in the pasture site the average height was ~0.25 m. Leaf area index (LAI, dimensionless) estimates were made with a LiCor LAI2000 instrument and are listed in Table 1. At site ER09 the eddy-covariance instrument tower was located in a particularly wet portion of the field, which was somewhat unrepresentative of the area as a whole.

[29] On each tower, a Campbell Scientific (company and trade names are given for the benefit of the reader and imply no endorsement by the USDA or University of Wisconsin) three-dimensional sonic anemometer and krypton hygrometer were positioned at a nominal height of 2 m agl for estimating the sensible (H) and latent (LE) heat fluxes. Wind speed, air temperature, and humidity measurements were made at approximately 2.5 m agl, and net radiation (R_n) was measured at approximately 2 m agl. The soil heat (G) flux at the surface was estimated by a combination of soil calorimetry and measurement of the heat-flux density at a nominal depth of 8 cm using an array of several heat flow transducers with the change in heat storage of the soil layer above the plate estimated using soil temperature measurements at nominal depths of 2 and 6 cm. Everest Interscience infrared radiometers (Model 4000 with a 60° field of view) were positioned approximately 2 m agl to measure radiometric surface temperature, $T_{RAD}(\phi)$, at a nadir viewing angle ($\phi = 0°$). Fluxes and meteorological variables were averaged to one-half hour.

[30] Further details on the reliability of surface flux observations made by eddy-covariance techniques are described by *Twine et al.* [2000]. A key finding of this study was that the sum of eddy covariance measurements of the turbulent heat fluxes, H and LE, were consistently less than the available energy, namely, $R_n - G$. This lack of closure in the surface energy balance ranged from 10 to 30% as quantified by taking the ratio of $(H + LE)/(R_n - G)$, suggesting that when measurement errors in available energy are known and modest, the eddy-covariance measurements of sensible and latent heat fluxes should be adjusted to obtain closure. All fluxes reported here have been corrected for such closure errors by modifying H and LE such that they summed to the available energy $(R_n - G)$ yet retained the observed Bowen ratio [*Twine et al.*, 2000].

[31] For comparison purposes, the DisALEXI model was also run with local inputs taken from a nearby station in the Oklahoma Mesonet [*Brock et al.*, 1995], a relatively dense network of meteorological stations (as opposed to the synoptic data inputs used in the first DisALEXI experiment). The wind speed observations from all Mesonet stations are available at the World Meteorological Organization (WMO) recommended 10 m agl, as is air temperature at 1.5 m, with some stations also having an air temperature measurement at 9 m agl. Details concerning Mesonet measurements and data quality control are described by *Shafer et al.* [2000].

3.2. Remote-Sensing Observations

3.2.1. Coarse Spatial Resolution Data

[32] In this experiment, the coarse-resolution surface temperature observations used in ALEXI were obtained with the GOES 8 imager instrument within the 10.2–11.2 μm (band 4) longwave infrared window. Thermal imager data are available every 15 min at a nadir-viewing angle of 39 degrees and a nominal spatial resolution of 5 km at the location of the SGP97 study area. Atmospheric correction of the GOES data was performed using MODTRAN [*Berk et al.*, 1998].

3.2.2. High Spatial Resolution Data

[33] High-resolution surface radiometric temperature, vegetation cover, and land-use maps were derived from

Table 1. Description of El Reno Flux Station Sites

Station	Leaf Area Index	Description
ER01	4.2	rangeland
ER05	2.6	rangeland
ER09	2.7	pasture
ER13	0	harvested winter wheat/tilled bare soil

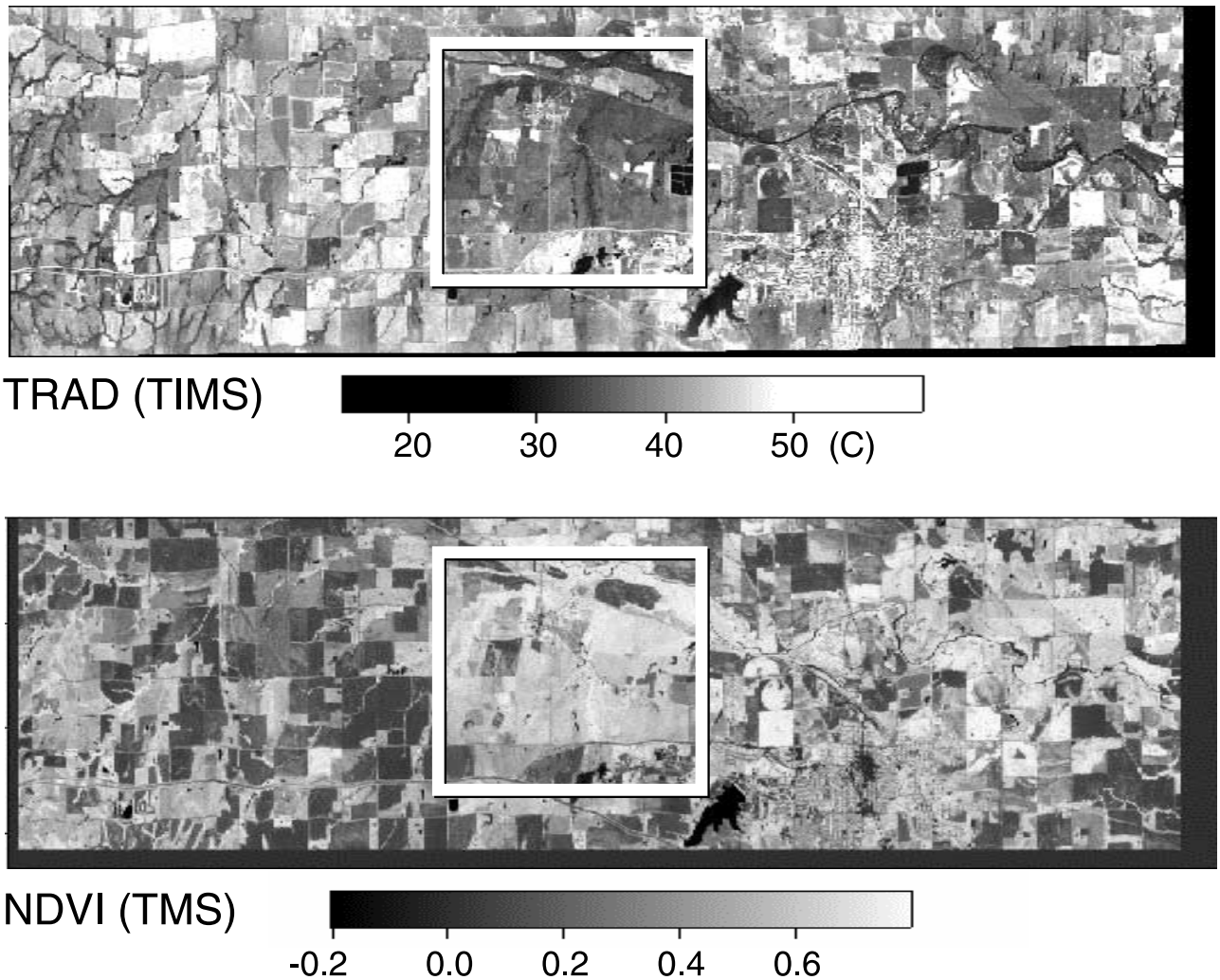

Figure 3. Maps at 24-m resolution of surface radiometric temperature derived from TIMS data (top) and NDVI from TMS observations (bottom) taken on 2 July 1997 at approximately 1030 CST. The boxes signify the size and location of the GOES thermal pixel used in the disaggregation experiments described in the text.

measurements made with the thermal infrared multispectral scanner (TIMS) and the thematic mapper simulator (TMS), flown by aircraft over the El Reno site. The TIMS instrument [*Palluconi and Meeks*, 1985] is a six-channel scanner operating in the thermal infrared (8–12 μm) region of the electromagnetic spectrum, while TMS mimics the Landsat TM visible and near-infrared bands and was used to create maps of NDVI. Both sensors were flown on a DOE Cessna Citation aircraft at ~5 km agl, yielding a ground resolution of 12 m; the 12-m TIMS and TMS data were then aggregated to 24 m (by averaging four adjacent 12-m pixels together) to reduce registration errors between the two sensors. Viewing angles for the aircraft ranged from nadir (i.e., $\phi = 0°$) to $\phi = 25°$; hence the average sensor viewing angle was of the order of 10°. The El Reno flight lines provided coverage of an area approximately 8 km north-south by 28 km east-west. *French et al.* [2000b, 2000a] provide further details concerning the processing of these data, including corrections for emissivity and atmospheric effects. Additionally, a map of land use/land cover in the modeling domain was created by a supervised maximum-likelihood classification scheme using TMS imagery from 2 July 1997.

[34] Maps of surface radiometric temperature and NDVI at 24-m resolution for 2 July are shown in Figure 3. These images demonstrate the heterogeneity contained in this landscape, with typical length scales of 100–200m. The highlighted box delineates the 5-km GOES pixel containing the El Reno study area, used in the ALEXI component of the mapping procedure.

3.3. Study Period

[35] Both low- (GOES) and high- (aircraft) spatial resolution remote-sensing data were collected on three clear mornings during SGP97, on day of year (DOY) 180 (29 June), 182 (1 July), and 183 (2 July). These consisted of two GOES images at about 1.5 and 5.5 hours past sunrise and one TIMS overflight at about the time of the second GOES observation (~1030–1100 central standard time; see Figure 4). The TMS data used here were acquired on DOY 183.

[36] This 3-day sequence of remote-sensing surveys followed a heavy rainfall event (~60 mm) that occurred over

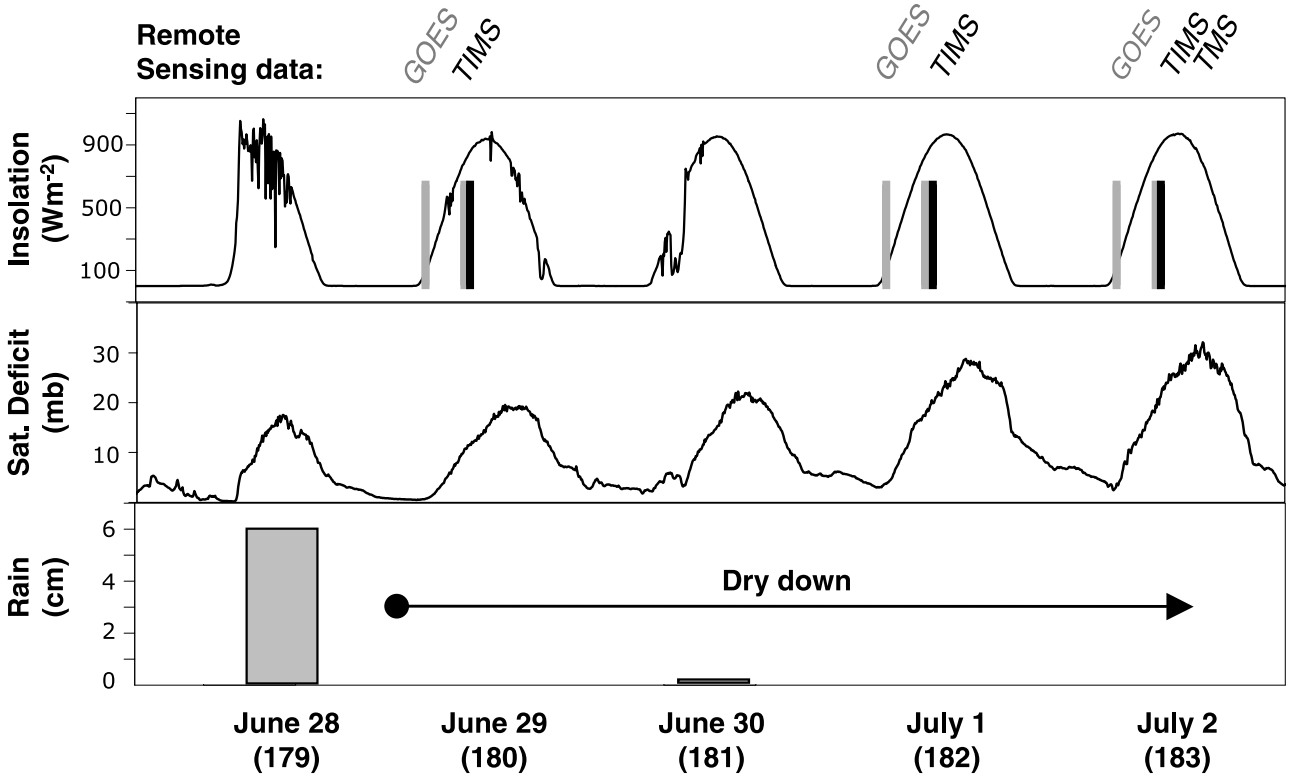

Figure 4. Time series of insolation, saturation deficit, and rainfall measurements acquired at the El Reno Mesonet station during the period of investigation. Also indicated are acquisition times for GOES, TIMS, and TMS images used for disaggregation.

the El Reno area on DOY 179. A general drying trend followed for the next several days, although there was a brief shower on DOY 181 adding another 1 mm of precipitation. Measurements from a nearby Mesonet station showed minor differences in solar radiation and air temperature between the 3 days around the time of the aircraft coverage (see Figure 4 and Table 2). The atmospheric saturation deficit, however, increased steadily over this interval (Figure 4), while soil moisture decreased. This dry-down period provided a valuable test of the sensitivity of the DisALEXI flux-mapping algorithm to changing surface and atmospheric conditions.

4. Results and Discussion

4.1. Instantaneous Fluxes

[37] Figure 5 shows a time series of surface temperature maps derived from the 24-m TIMS data for DOY 180, 182, and 183, acquired at approximately 1030 local standard time (LST). The warming that occurred during the dry-down is apparent, particularly in the bare fields of harvested winter wheat, where surface temperatures increase from ~30° to 50°C. Corresponding maps of latent heating at 1030 LST generated with DisALEXI are also shown in Figure 5. Estimated evapotranspiration rates in the bare fields are reduced dramatically as the soil surface dries. On the other hand, in the dense vegetation in the riparian zones around the network of streams to the north (probably transpiring at the potential rate on all three days), evaporation increases on DOY 182 and 183 when the atmospheric demand for water vapor is high.

[38] This general time behavior is supported by measurements made at four flux towers operating within El Reno study area (Figure 2). Figure 6 shows the latent heat flux observed at these flux stations at the time of the TIMS overpasses on the 3 study days, together with the 5-km

Table 2. Ambient Atmospheric and Surface Temperature Conditions, and ALEXI Flux Estimates for Targeted Modeling Days[a]

DOY	t_1, CST	t_2, CST	RH_2, %	$T_{a,2}$,C	W_2, m/s	ΔT_{RAD}, C	$R_{n,2}$, W m^{-2}	LE_2, W m^{-2}	H_2, W m^{-2}	G_2, W m^{-2}
180	6.25	10.75	72.9	29.0	6.0	9.0	671	475	95	101
182	6.25	10.75	60.0	30.5	6.3	13.7	676	410	175	92
183	6.25	10.25	60.6	30.3	2.7	16.6	602	343	187	72

[a]Here t_1 and t_2 are the acquisition times of the two thermal GOES images used in ALEXI; RH_2, $T_{a,2}$, and W_2 are the relative humidity, 9 m agl air temperature, and 10-m agl wind speed measured at the El Reno mesonet station at time t_2; ΔT_{RAD} is the surface temperature change at El Reno between times t_1 and t_2 as estimated from atmospherically corrected 5-km imagery from the GOES imager (band 4); and $R_{n,2}$, LE_2, H_2, and G_2 are flux estimates for El Reno from the ALEXI model at time t_2.

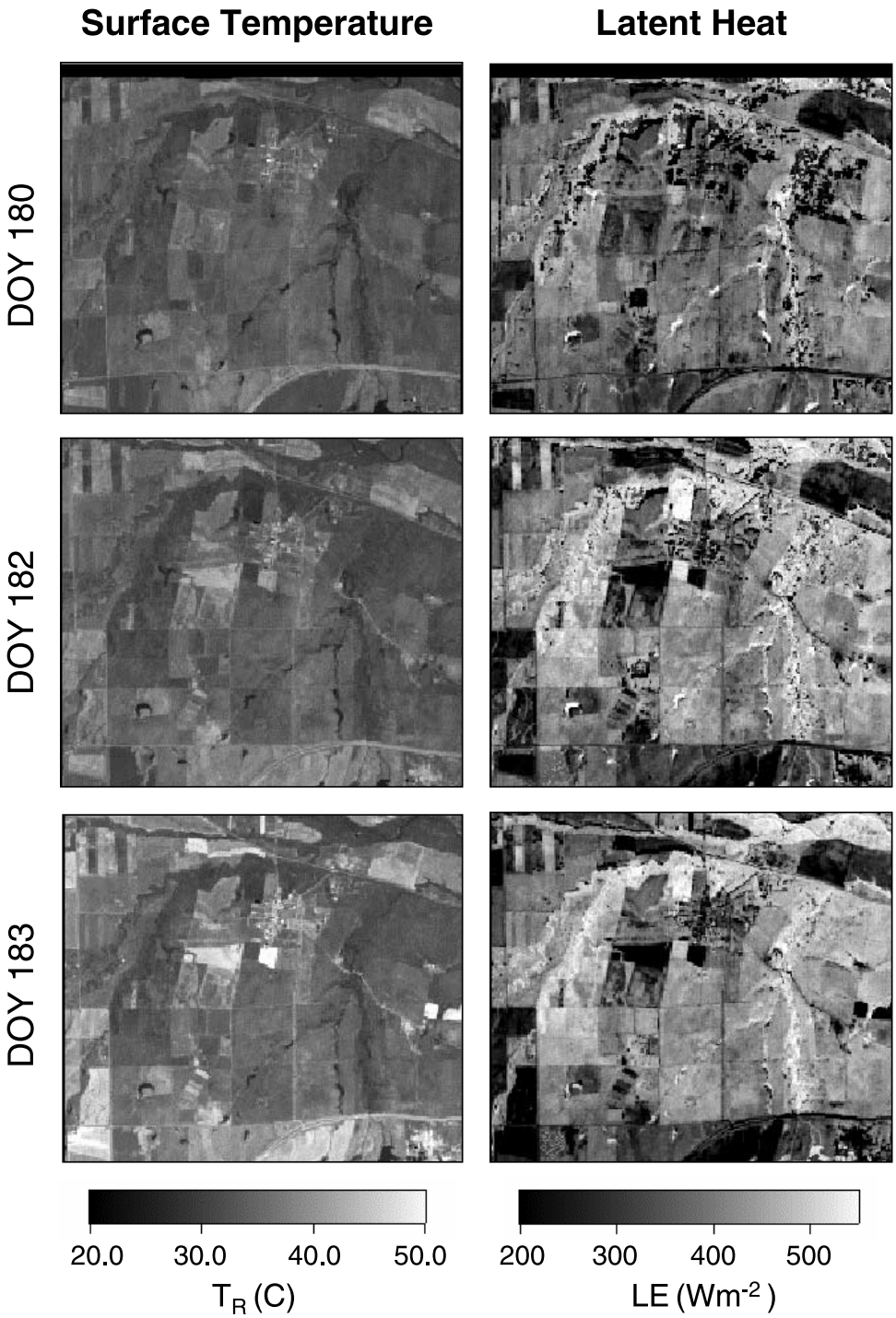

Figure 5. Maps at 24-m resolution of surface radiometric temperature (left) and disaggregated latent heat flux estimates (right) over the El Reno study area for DOY 180, 182, and 183. See color version of this figure at back of this issue.

ALEXI estimate. The latent heat flux at the site with the densest vegetation cover (ER01) increases slightly on DOY 182 and 183, while the evaporation from the bare field site (ER13) drops steadily after the rainfall event on DOY 179. The two sites with intermediate vegetative cover, which are not significantly different in cover, fall between ER01 and ER13 in their behavior. The 5-km ALEXI latent heat fluxes decrease monotonically, reflecting the likely influence of the bare soil/harvested winter wheat fields present within the scene (Figure 3).

[39] Figure 7 contains a comparison of tower measurements with DisALEXI model predictions of the four major flux components extracted at the locations of the flux towers. To account for variations in fetch influencing fluxes observed at the height of the eddy correlation instrument (2 m agl), the 24-m flux predictions were re aggregated

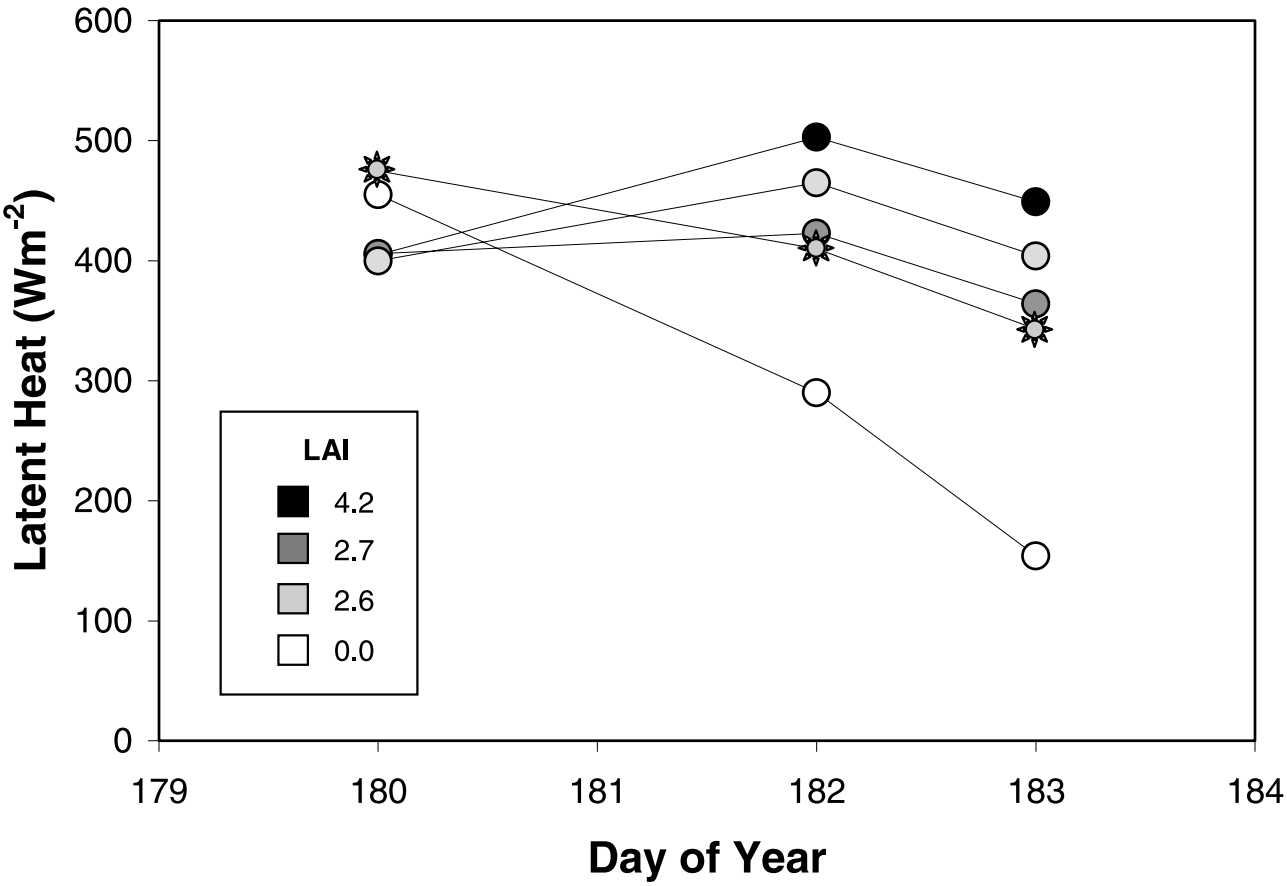

Figure 6. Latent heat flux observed at four eddy-covariance flux towers in El Reno at the time of the TIMS overpasses on DOY 180, 182, and 183. Stars indicate ALEXI 5-km latent heat flux estimates for these times.

to a scale of ~100 m using the analytical footprint analysis technique of *Scheupp et al.* [1990]. This constituted a weighted average of approximately 12 pixels upwind of the tower location. Figure 7 shows that the decrease in latent heating observed at the bare-soil site is captured by the DisALEXI model, while the vegetated sites show more constant evaporation rates throughout the dry-down period. For all flux components, the root-mean-square deviation (RMSD) between model estimates and measurements is 38 W m^{-2}. This compares well with the observational accuracy of 20–40 W m^{-2} typically associated with eddy-covariance flux measurements (see *Norman et al.* [1995b, p. 281] for discussion; see also *Twine et al.* [2000]).

[40] To ascertain the utility of ALEXI in providing reasonable estimates of air temperature at 50 m, used as the upper boundary condition in phase 2 of the disaggregation (Figure 1), a second disaggregation was performed using a local measurement of air temperature at a height of 9 m agl, taken at a Mesonet station in the El Reno study area. Footprint-weighted flux estimates from DisALEXI are compared with observations in Figure 8, with an overall RMSD of 39 W m^{-2}. This accuracy is similar to that from the experiment using ALEXI-derived air temperatures shown in Figure 7, which had the operational advantage that no on-site measurements were used.

[41] The importance of disaggregating regional scale flux estimates down to scales consistent with the flux observations used for validation is further evidenced in Figure 6, where the 5-km ALEXI flux predictions for the 3 study days are compared with observed fluxes. On DOY 183, for example, observed ET fluxes varied from 200 to 500 W m^{-2}, while the ALEXI 5-km flux was 343 W m^{-2}. A simple average of the four local sites agrees reasonably well with ALEXI. This is purely fortuitous, however; these four sites happen to be representative of the heterogeneity of the larger 5-km pixel in this particular case. In general, subpixel heterogeneity in surface properties, such as vegetation cover and soil moisture, leading to significant surface temperature contrasts within a scene can serve to corrupt flux estimates based on pixel-average model input parameters [*Kustas and Norman*, 2000]. Combining this issue with the fact that typically only a single flux tower site would be available for validation, it is obvious that comparisons between kilometer-scale modeled fluxes and 100-m scale tower observations contain large uncertainties, providing little in the way of assurance in the utility of the remote-sensing model for mapping fluxes across a landscape. In fact, the location of the flux tower and how it reflects average conditions over the remotely sensed scene would largely determine the level of agreement between the remote-sensing model output and the measurements, even if the model were very reliable. The variability in modeled heat fluxes at the 24-m resolution over the 5-km pixel is much larger than the root-mean-square difference between DisALEXI fluxes and the in situ

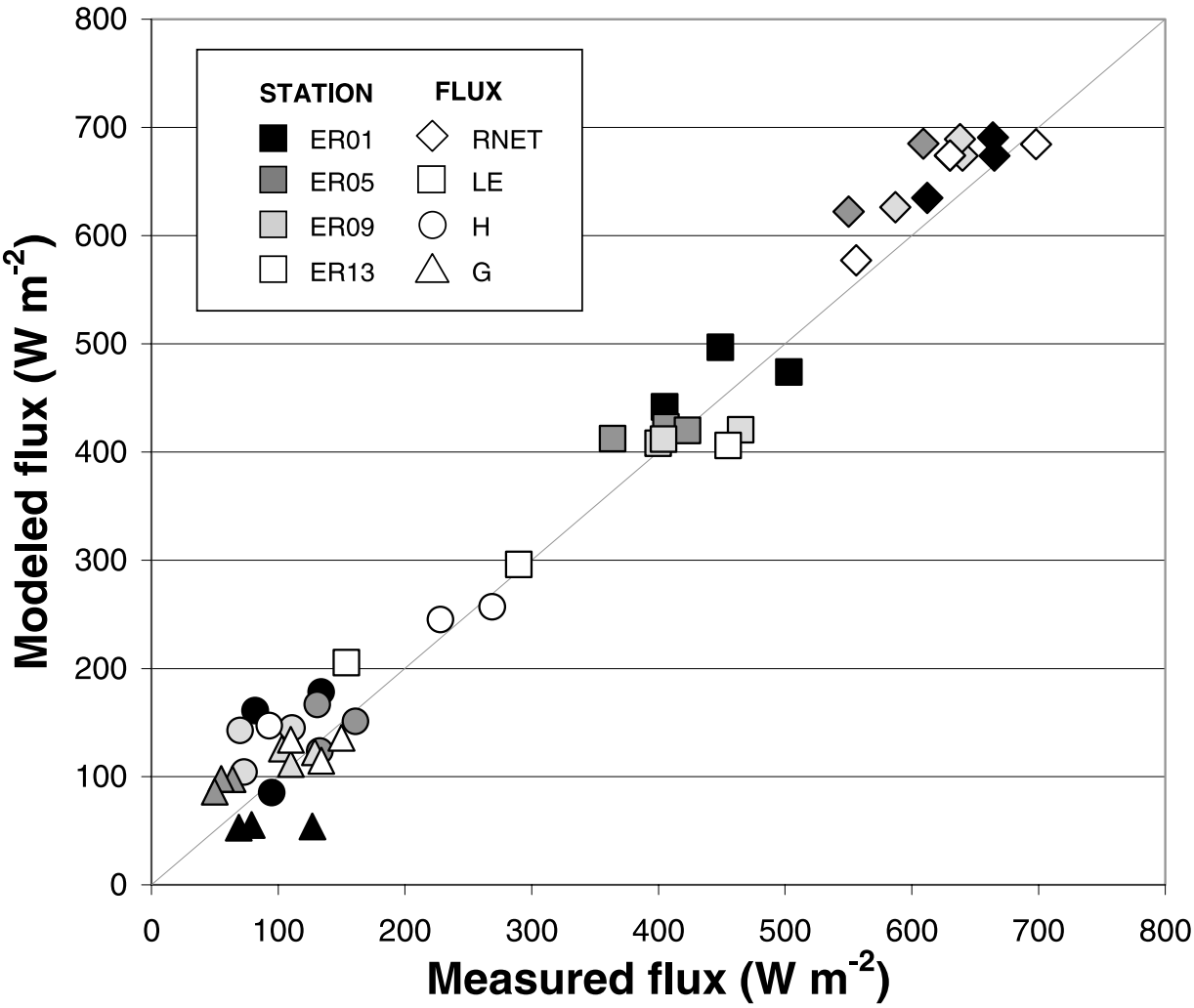

Figure 7. Comparison of energy budget component measurements from four flux towers with instantaneous flux estimates (~1030 CST) from the DisALEXI disaggregation algorithm. In this experiment, the upper boundary condition in air temperature (at 50 m agl) was provided by the ALEXI model (as in Figure 1).

surface flux measurements, suggesting that a high-resolution approach is important for validation at this Oklahoma site.

4.2. Daytime Extrapolation of Instantaneous Flux Estimates

[42] Figures 5–8 compare instantaneous fluxes that were modeled/measured at the time of the aircraft overpass and the second GOES image, about 1030 LST. Assuming the relative partitioning of the energy budget remains constant throughout the day, these instantaneous flux estimates can be used to predict hourly and daily-integrated fluxes, which will be of greater utility in many applications. Field studies have shown that the "evaporative fraction" (EF), given by the ratio between latent heat and the available energy flux ($LE/(R_n - G)$), is generally relatively stable during the daytime hours and can be used to extrapolate the single snapshots of surface conditions typically afforded by remote sensing to longer timescales [e.g., *Sugita and Brutsaert*, 1991; *Brutsaert and Sugita*, 1992; *Hall et al.*, 1992; *Anderson et al.*, 1997].

[43] Half-hourly flux estimates for DOY 183 at the four El Reno sites are shown in Figure 9, generated assuming the evaporative fraction predicted by DisALEXI at 1030 LST remained constant throughout the day. Here the shortwave component of hourly net radiation was estimated using a clear-sky radiative transfer model and a cover-dependent surface albedo [*Campbell and Norman*, 1998], while the net longwave component was held constant at the modeled 1030 LST value. The sensible and latent heat fluxes were then estimated from the available energy, $R_n - G$, assuming a constant evaporative fraction for each day.

[44] The soil heat conduction flux is often estimated as a fraction of the net radiation at the soil surface [*Choudhury et al.*, 1987; *Norman et al.*, 1995b; *Anderson et al.*, 1997]; however, this can produce large errors in afternoon instantaneous fluxes when the net radiation and soil conduction flux curves are out of phase. In Figure 9 the half-hourly soil heat fluxes were approximated with an analytical solution to the soil heat conduction equation for a homogeneous media with a sinusoidal boundary

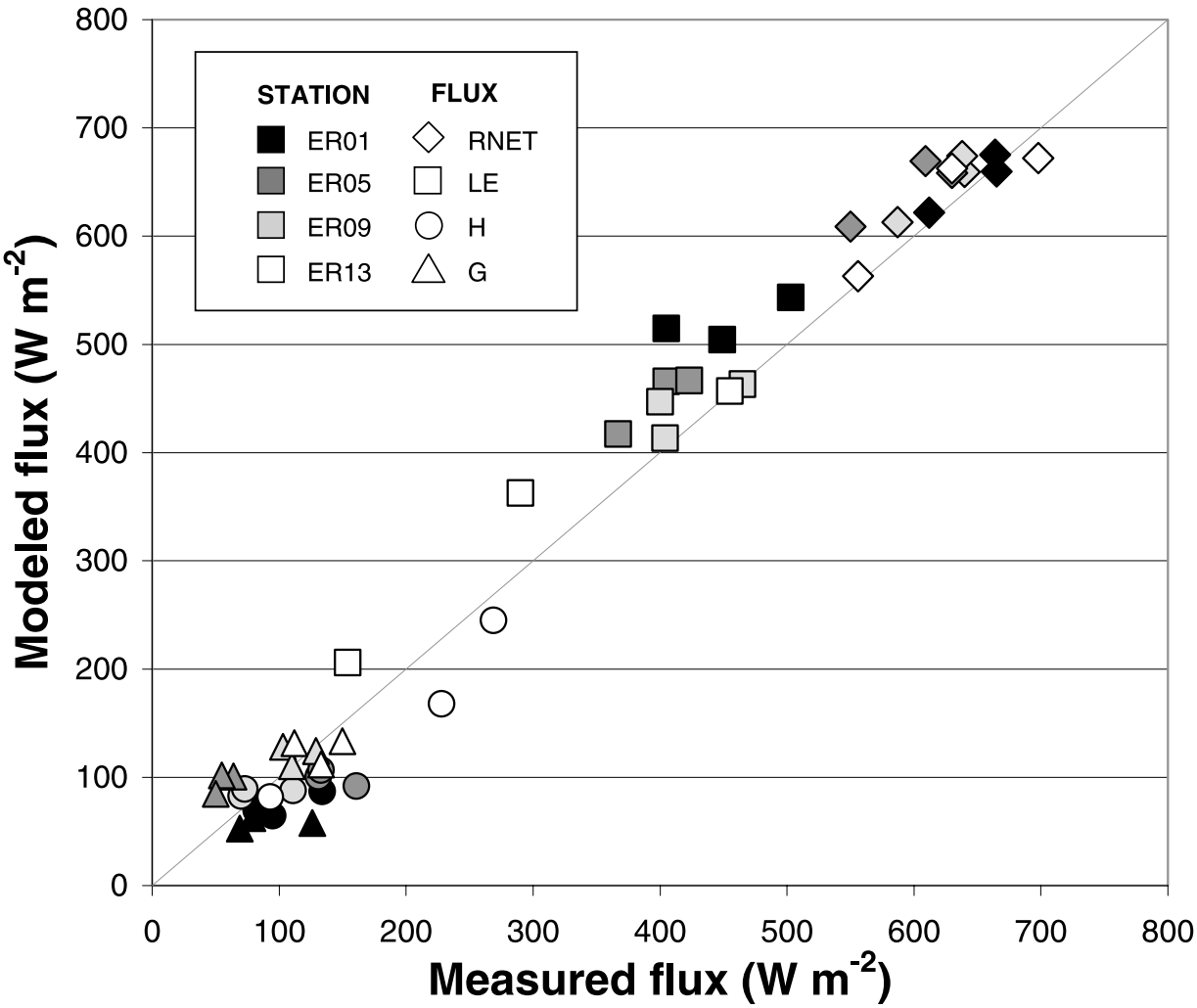

Figure 8. Comparison of energy budget component measurements at four flux towers with instantaneous flux estimates (~1030 CST) from the DisALEXI disaggregation algorithm. In this experiment, a local measurement of air temperature at 9 m agl from the El Reno Mesonet station was used as the upper boundary condition in DisALEXI.

condition [see, e.g., *Campbell and Norman*, 1998]; namely,

$$G(t) = G(t_2)\frac{\sin[\omega(t - t_o) + \pi/4]}{\sin[\omega(t_2 - t_o) + \pi/4]}$$

where $G(t)$ is the soil conduction flux at some time t during the day, $G(t_2)$ is the soil conduction flux from DisALEXI at time t_2 (~1030 LST), t_o is the time when the first harmonic of the soil conduction flux curve passes through zero in the morning hours, and ω is 2π radians/24 hours. If $t_o = 8$ hours, then the maximum of the soil heat conduction flux occurs at 1100 LST and the soil flux is again zero at 1700 LST. This means that t_2 is very near the time of maximum soil heat conduction flux. This simple solution just normalizes soil conduction fluxes throughout the day to the flux predicted by DisALEXI at t_2, preserving the normal phase that soil heat flux has relative to solar radiation. For different day lengths, t_o may change slightly and can be adjusted by relating to sunrise and sunset.

[45] The results of this simple method for estimating hourly surface fluxes are encouraging for both the vegetated (ER01, ER05, and ER09) and nonvegetated (ER13) sites, although some significant errors are present (Figure 9). Estimates of R_n and G generally agree with measurements to within 50 W m^{-2}, yielding a relative error of less than 10% for R_n, but a much larger relative error for G (~50%). However, this translates to only a ~10% relative error in available energy, $R_n - G$. Estimates of H and LE agree with measurements to within 50 W m^{-2} before local noon, yielding an average relative error of less than 20%, with larger errors in the afternoon.

[46] The measurements suggest that ambient conditions changed at about 1300 LST, resulting in a small but steady increase in the evaporative fraction toward sunset for the vegetated sites, while the bare soil site ER13 shows a decline, likely due to drying of the soil surface (Figure 10). While the morning EF is generally adequately modeled, subsequent changes, due to surface drying or increasing evaporative demand, cannot be captured by a single morning snapshot of surface conditions. This can lead to a deterioration in the model predictions as the day progresses, as evident in Figure 9. Discrepancies are par-

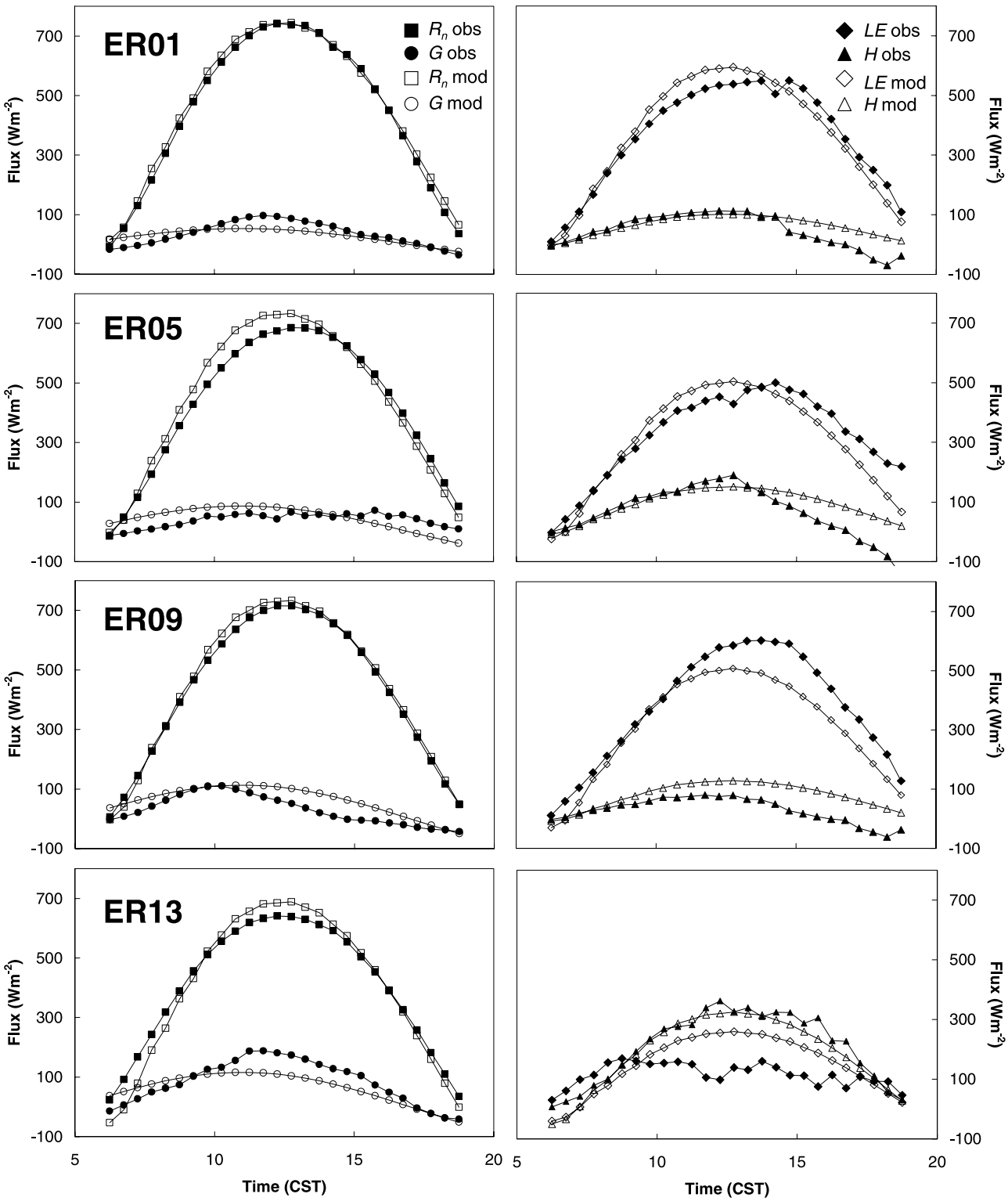

Figure 9. Hourly flux estimates, extrapolated from instantaneous values predicted by the DisALEXI model at 1030 CST by assuming a constant evaporative fraction, compared with measurements made at four flux towers on DOY 183.

ticularly marked at sites ER09 and ER13, where the error in the DisALEXI prediction of morning EF is in the direction opposite to the observed afternoon trend. The flux station at ER09 was located in an unrepresentatively wet part of the field, and thus uncertainties in image registration and footprint analysis, and subpixel heterogeneity are likely contributing to the larger errors evident there. If high-resolution thermal images were available at multiple times during a given day, diurnal trends in EF could potentially be modeled. The nominal times corresponding to Terra and

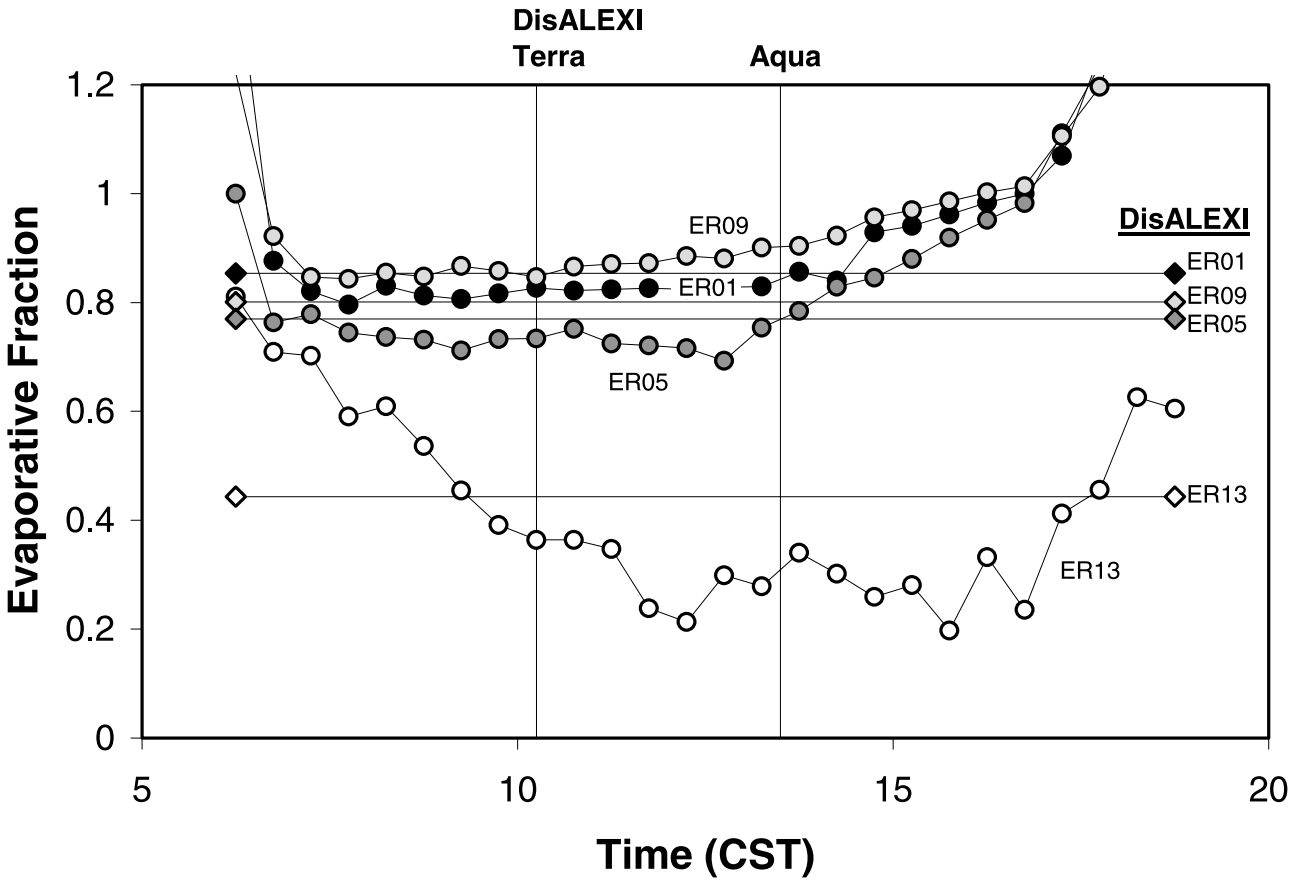

Figure 10. Hourly observations of the evaporative fraction (EF) made at four flux towers in El Reno on DOY 183. Also plotted are EFs predicted by the DisALEXI model at these sites at ~1030 CST. The strategy described in the text for extrapolating instantaneous flux estimates to daytime totals assumes EF is constant through the day. The times of MODIS overpasses on the Terra and Aqua satellites are also indicated. A second thermal image, acquired at 1330 CST, may assist in identifying diurnal trends in EF.

Aqua satellite overpasses are indicated in Figure 10. A second MODIS image at ~1330 LST could provide useful EF time trend information, particularly for sites exhibiting moisture stress, such as ER13.

[47] Modeled and measured daily integrated surface fluxes for DOY 183 agree to within 1–1.5 MJ m^{-2} d^{-1} (5–8% of the net radiation flux), except at ER09 where latent heating is underestimated by 3 MJ m^{-2} d^{-1} and H is overestimated by 2.5 MJ m^{-2} d^{-1} (Figure 11). Results for the other 2 days were similar (not shown).

5. Conclusions

[48] The DisALEXI flux disaggregation approach described in this paper has been developed to combine low- and high-resolution remote sensing data to estimate surface fluxes on the 10^1–10^2 m scale without requiring any local observations. The algorithm was tested with ground-based eddy-covariance flux measurements collected in a rangeland landscape near El Reno, Oklahoma. For all flux components, the root-mean-square deviation (RMSD) between model estimates and measurements was 40 W m^{-2}, comparable with the observational accuracy typically associated with micrometeorological flux measurement techniques. Further validation over different landcover types is required before the general utility of DisALEXI can be assessed. This work is in progress. In principle, this technique has many practical advantages that warrant further investigation:

[49] 1. DisALEXI uses only inputs that are readily available and therefore may be useful for routine flux monitoring applications where continuous, on-site data collection is not possible.

[50] 2. The models used have been designed to be fairly robust to expected errors in the calibration and correction of the remote sensing data [*Anderson et al.*, 1997].

[51] 3. Disaggregation may provide a means of validating regional-scale flux models, like ALEXI, over heterogeneous landscapes where direct comparison to ground-based measurements may be invalid. The level of agreement between the disaggregated fluxes and point surface observations noted in this study, for example, gives us some confidence that the 5-km aggregated flux estimates from ALEXI were reasonable in this case.

[52] Studies are currently under way which may expand the utility and robustness of DisALEXI disaggregation products. For many high-resolution satellites, such as ASTER, Landsat, and MODIS, the visible and near-infrared wavebands are sampled at 2–6 times higher spatial resolution than the thermal band. A new technique has

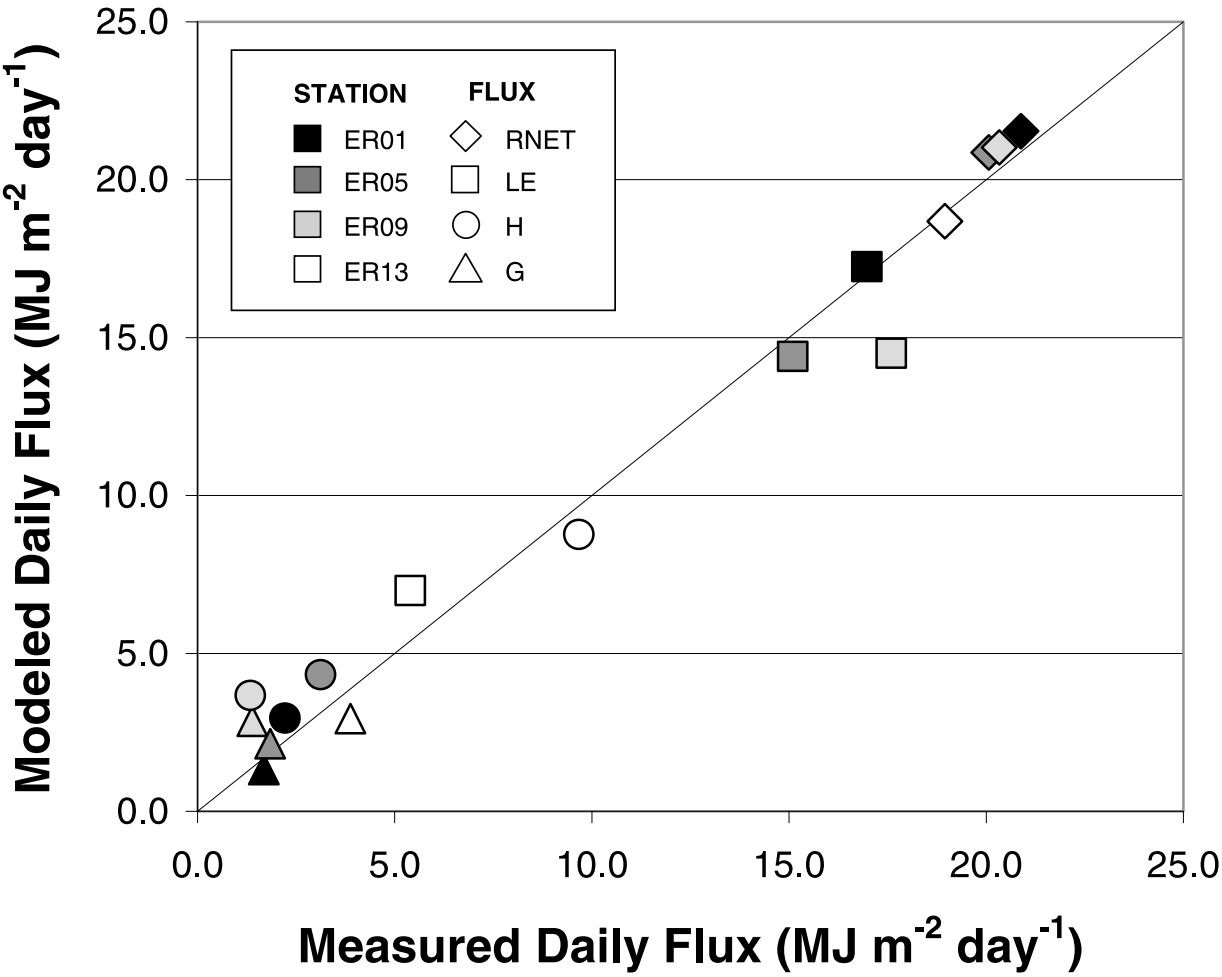

Figure 11. Comparison of DisALEXI predictions of daytime total surface fluxes with time-integrated measurements made at four flux towers on DOY 183.

been developed recently for sharpening thermal images to visible/NIR resolutions, exploiting the relationship between vegetation indices and surface radiometric temperature [*Kustas et al.*, 2003]. We are also exploring ways in which a second, afternoon thermal image could be used in the disaggregation procedure as a means for identifying diurnal trends in the evaporative fraction. Work has commenced on implementing an analytical canopy resistance submodel [*Anderson et al.*, 2000] within the two-source remote-sensing framework. This will potentially improve model estimates of canopy transpiration and enable mapping of carbon assimilation fluxes at high spatial resolution. Finally, simulations from a large-eddy simulation model with a two-source land-surface representation are providing information regarding the scale dependence of coupling between spatial variability in surface conditions and temperature in the lower atmosphere [*Albertson et al.*, 2001]. Recent work conducted with the LES involved artificially varying the contrast in a remotely sensed surface temperature field and evaluating differences in the spatially distributed fluxes from the two-source model flux estimates using as uniform surface layer air temperature and wind speed versus the fully coupled LES over the modeling domain [*Kustas and Albertson*, 2003]. Such experiments will be valuable in assessing the implications of assuming a uniform air temperature at the blending height over a heterogeneous surface.

Appendix A: The ALEXI Model

A1. The Two-Source Surface Model Component

[53] The two-source model (TSM) [*Norman et al.*, 1995b] is a variant of the two-layer surface representation first suggested by *Shuttleworth and Wallace* [1985] as a means to bridge the gap between surface temperature, a quantity that can be remotely sensed, and aerodynamic temperature, a hypothetical quantity that solves the bulk surface sensible heat flux equation (see discussion by *Norman et al.* [1995b]).

[54] The TSM partitions the composite surface radiometric temperature (T_{RAD}) of a scene into soil and canopy contributions (T_s and T_c, respectively), based on the fraction of vegetation cover apparent when the surface is viewed at angle ϕ from nadir ($f(\phi)$). The set of equations in the TSM defining energy fluxes of net radiation (R_n), sensible (H), latent (LE) and soil heating (G) is as follows (see Figure 1):

Surface radiometric temperature at view angle ϕ

$$T_{RAD}(\phi) \approx f(\phi)T_c + [1 - f(\phi)]T_s \qquad \text{(A1)}$$

Vegetation cover fraction viewed at nadir and at angle ϕ assuming a spherical leaf angle distribution

$$f_c = 1 - \exp(-0.5F) \tag{A2}$$

$$f(\phi) = 1 - \exp\left(\frac{-0.5F}{\cos\phi}\right) \tag{A3}$$

Soil, canopy, and system energy budgets

$$R_n = H + LE + G \tag{A4}$$

$$R_{n,s} = H_s + LE_s + G \tag{A5}$$

$$R_{n,c} = H_c + LE_c \tag{A6}$$

Net radiation

$$R_n = R_{n,s} + R_{n,c} \tag{A7}$$

$$\begin{aligned} R_n &= (L_d - L_u) + (S_d - S_u) \\ &= L_d - (1-\tau_c)L_c - \tau_c L_s + (1-A)S_d \end{aligned} \tag{A8}$$

$$\begin{aligned} R_{n,s} &= \left(L_{d,s} - L_{u,s}\right) + \left(S_{d,s} - S_{u,s}\right) \\ &= \tau_c L_d + (1-\tau_c)L_c - L_s + (1-\rho_s)S_{d,s} \end{aligned} \tag{A9}$$

Sensible heat

$$H = H_s + H_c = \rho c_p \frac{T_{ac} - T_a}{R_a} \tag{A10}$$

$$H_s = \rho c_p \frac{T_s - T_{ac}}{R_s} \tag{A11}$$

$$H_c = \rho c_p \frac{T_c - T_{ac}}{R_x} \tag{A12}$$

Latent heat

$$LE = LE_s + LE_c \tag{A13}$$

$$LE_c = \alpha_{PT} f_g \frac{S}{S+\gamma} R_{nc} \tag{A14}$$

Soil conduction heat

$$G = 0.3R_{n,s} \tag{A15}$$

where T is temperature, R is a transport resistance, F is the leaf area index, ρ is air density, c_p is the heat capacity of air at constant pressure, γ is the psychometric constant, α_{PT} is an adjustable Priestley-Taylor [*Priestley and Taylor*, 1972] coefficient (see below), f_g is the fraction of green vegetation in the scene, and S is the slope of the saturation vapor pressure vs. temperature curve. The subscripts a, ac, and x signify properties of the air above and within the canopy, and within the leaf boundary layer, respectively, while s and c refer to fluxes and states associated with the soil and canopy components of the system. The soil heat conduction flux is computed as a simple function of the net radiation at the soil surface [*Choudhury et al.*, 1987].

[55] The resistance formalism described here allows both the soil and the vegetation to influence the microclimate within the canopy air space, as shown in Figure 1. The resistances considered include R_a, the aerodynamic resistance between the canopy and the upper boundary of the model (including diabatic corrections); R_x, the bulk boundary layer resistance over all leaves in the canopy; and R_s, the resistance through the boundary layer immediately above the soil surface. Mathematical expressions for these resistance terms are given by *Norman et al.* [1995b]. In computing R_a, the surface aerodynamic roughness is estimated from the height of the dominant vegetation in the scene [*Massman*, 1997].

[56] In equations (A1)–(A15), R_n is the net radiation above the canopy, $R_{n,c}$ is the component absorbed by the canopy, and $R_{n,s}$ is the component penetrating to the soil surface. Here the longwave components of R_n and $R_{n,s}$ are a function of the thermal radiation from the sky (L_d), the canopy (L_c) and the soil (L_s), and the coefficient of diffuse radiation transmission through the canopy (τ_c). The shortwave components depend on insolation values above the canopy (S_d) and above the soil surface ($S_{d,s}$), and the reflectivity of the soil-canopy system (A) and the soil surface itself (ρ_s). *Campbell and Norman* [1998] provide approximations for τ_c depending on leaf absorptivity and leaf area index.

[57] The coefficient α_{PT} governing the canopy transpiration rate is adjusted if the potential transpiration rate in equation (A14) overestimates the actual transpiration, e.g., during conditions of vegetative stress. When stress occurs, T_{rad} and thus H will be large. Initial passes through the equation set will yield a negative soil evaporation rate (which is computed as a residual) to compensate for the unreasonably high transpiration rate estimate. Condensation onto the soil near noontime is unlikely, so such cases are trapped and further iterations progressively throttle α_{PT} back until the soil evaporation approaches zero (as expected under dry conditions). See *Kustas et al.* [2003] for further details.

A2. The Atmospheric Boundary Layer (ABL) Model Component

[58] Reliable upper boundary conditions in air temperature for the two-source model are difficult to obtain with adequate accuracy over regional scales. The ALEXI model uses a simple atmospheric boundary layer (ABL) closure technique to evaluate the morning evolution of air temperature in the surface layer, given estimates of time-integrated sensible heat influx provided by the TSM. This effectively moves the model upper boundary conditions from just above the canopy up to the height of the ABL, of the order of a kilometer above the Earth's surface (see Figure 1). At

this height, atmospheric temperatures are less tightly coupled to local surface conditions and thus can be specified with greater accuracy over large regions with radiosonde and satellite soundings.

[59] The primary forcing input to the ALEXI model is the time change in radiometric surface temperature, derived from two thermal satellite images acquired during the morning hours. Time changes in surface temperature are found to be well correlated with the partitioning between sensible and latent heating fluxes; wetter surfaces warm more slowly and expend more energy in evaporation. Furthermore, the use of time-differential temperature measurements rather than single measurements reduces errors due to sensor calibration and assumptions concerning surface emissivity.

[60] Using brightness temperature measurements acquired at two times during the morning (t_1 and t_2), and initial estimates of near-surface air temperature, the TSM (equations (A1)–(A15)) yields instantaneous sensible heat flux estimates H_1 and H_2. Assuming a linear functional form for $H(t)$, a time-integrated heat flux can be obtained:

$$\int_{t_1}^{t_2} H(t)dt = \frac{1}{2}[H_2 t_2 - H_1 t_1]. \tag{A16}$$

[61] The air temperature estimates are constrained by a simple slab model describing planetary boundary layer dynamics. *McNaughton and Spriggs* [1986] give a conservation equation relating the rise in height (z) and potential temperature (θ_m) of the mixed layer to the time-integrated sensible heating from the surface:

$$\int_{t_1}^{t_2} H(t)dt = \rho c_p(z_2\theta_{m2} - z_1\theta_{m1}) - \rho c_p \int_{z_1}^{z_2} \theta_s(z)dz \tag{A17}$$

where $\theta_s(z)$ is the early morning potential temperature profile.

[62] Near the land surface, the mixed layer potential temperature and the air temperature are related by

$$\theta_m = T_a\left(\frac{100}{p}\right)^{R/c_p} \tag{A18}$$

where p is the atmospheric pressure (in kPa) and R/c_p = 0.286. The surface and boundary layer components of the model iterate until the time-integrated sensible heat flux estimates from both components converge. *Anderson et al.* [1997] provide further details concerning the solution sequence used in the ALEXI model.

[63] Primary remote sensing inputs to ALEXI include the morning time-rate-of-change in surface radiometric temperature (from GOES imager (5 km) or sounder (10 km) observations, atmospherically corrected using the methods of *French et al.* [2003]) downwelling solar and longwave radiation (to compute net radiation), and fractional vegetation cover (to deconvolve the composite surface temperature measurements into soil and canopy contributions). A landcover classification map derived from multispectral satellite data is used in conjunction with the cover-fraction map to assign class-dependent surface properties, such as surface roughness, albedo, and emissivity. Ancillary surface and atmospheric data required include an estimate of the wind speed field at 50 m and an early-morning analysis of synoptic radiosounding profiles of temperature and vapor pressure across the modeling domain. *Mecikalski et al.* [1999] review in detail the input requirements for regional-scale application of the ALEXI model.

[64] **Acknowledgments.** Funding for this research was provided primarily by NASA grant NAG13-99008 and in part by USDA Cooperative Agreement 58-1265-1-043. Suggestions and comments made by the anonymous reviewers greatly improved the clarity and overall presentation of the paper.

References

Albertson, J. D., W. P. Kustas, and T. M. Scanlon, Large-eddy simulation over heterogeneous terrain with remotely sensed land surface conditions, *Water Resour. Res.*, *37*, 1939–1953, 2001.

Anderson, M. C., J. M. Norman, G. R. Diak, W. P. Kustas, and J. R. Mecikalski, A two-source time-integrated model for estimating surface fluxes using thermal infrared remote sensing, *Remote Sens. Environ.*, *60*, 195–216, 1997.

Anderson, M., J. M. Norman, T. P. Meyers, and G. R. Diak, An analytical model for estimating canopy transpiration and carbon assimilation fluxes based on canopy light-use efficiency, *Agric. For. Meteorol.*, *101*, 265–289, 2000.

Anton, J. A., and J. A. Ross, Emissivity of the vegetation-soil system (in Russian, with English summary), *Sov. J. Remote Sens.*, *5*, 49–55, 1987.

Berk, A., L. S. Bernstein, G. P. Anderson, P. K. Acharya, D. C. Robertson, J. H. Chetwynd, and S. M. Adler-Golden, MODTRAN cloud and multiple scattering upgrades with application to AVIRIS, *Remote Sens. Environ.*, *65*, 367–375, 1998.

Blyth, E. M., Using a simple SVAT scheme to describe the effect of scale aggregation, *Boundary Layer Meteorol.*, *72*, 267–285, 1995.

Brock, F. V., K. C. Crawford, R. L. Elliott, G. W. Cuperus, S. J. Stadler, H. L. Johnson, and M. D. Eilts, The Oklahoma Mesonet: A technical overview, *J. Atmos. Oceanic Technol.*, *12*, 5–19, 1995.

Brutsaert, W., On a derivable formula for long-wave radiation from clear skies, *Water Resour. Res.*, *11*, 742–744, 1975.

Brutsaert, W., and M. Sugita, Application of self-preservation in the diurnal evolution of the surface energy budget to determine daily evaporation, *J. Geophys. Res.*, *97*, 18,377–18,382, 1992.

Campbell, G. S., and J. M. Norman, *An Introduction to Environmental Biophysics*, Springer-Verlag, New York, 1998.

Carlson, T. N., Regional-scale estimates of surface moisture availability and thermal inertia using thermal measurements, *Remote Sens. Rev.*, *1*, 197–247, 1986.

Carlson, T. N., J. K. Dodd, S. G. Benjamin, and J. N. Cooper, Satellite estimation of the surface energy balance, moisture availability and thermal inertia, *J. Appl. Meteorol.*, *20*, 67–87, 1981.

Choudhury, B. J., S. B. Idso, and R. J. Reginato, Analysis of an empirical model for soil heat flux under a growing wheat crop for estimating evaporation by an infrared-temperature-based energy balance equation, *Agric. For. Meteorol.*, *39*, 283–297, 1987.

Choudhury, B. J., N. U. Ahmed, S. B. Idso, R. J. Reginato, and C. S. T. Daughtry, Relations between evaporation coefficients and vegetation indices studied by model simulations, *Remote Sens. Environ.*, *50*, 1–17, 1994.

Claussen, M., Flux aggregation at large scales: On the limits of validity of the concept of blending height, *J. Hydrol.*, *166*, 371–382, 1995.

Divakarla, M. G., Estimating spatially distributed surface fluxes from satellite data, in-situ measurements and the Cupid model using GIS, Ph.D., thesis, Univ. of Wisc.-Madison, 1997.

French, A. N., T. J. Schmugge, and W. P. Kustas, Discrimination of senescent vegetation using thermal emissivity contrast, *Remote Sens. Environ.*, *74*, 249–254, 2000a.

French, A. N., T. J. Schmugge, and W. P. Kustas, Surface fluxes over the SGP site with remotely sensed data, *Phys. Chem. Earth*, *25*, 167–172, 2000b.

French, A. N., J. M. Norman, and M. C. Anderson, Simplified correction of GOES thermal infrared observations, *Remote Sens. Environ.*, in press, 2003.

Friedl, M. A., Relationships among remotely sensed data, surface energy balance, and area-averaged fluxes over partially vegetated land surfaces, *J. Appl. Meteorol.*, *35*, 2091–2103, 1996.

Gao, W., R. L. Coulter, B. M. Lesht, J. Qiu, and M. L. Wesely, Estimating clear-sky regional surface fluxes in the southern Great Plains atmospheric

radiation measurement site with ground measurements and satellite observations, *J. Appl. Meteorol.*, *37*, 5–22, 1998.

Gardner, B. R., D. C. Nielsen, and C. C. Shock, Infrared thermometry and the crop water stress index, II, Sampling procedures and interpretation, *J. Prod. Agric.*, *5*, 466–475, 1992.

Gillies, R. R., J. Cui, T. N. Carlson, W. P. Kustas, and K. S. Humes, Verification of a method for obtaining surface soil water content and energy fluxes from remote measurements of NDVI and surface radiant temperature, *Int. J. Remote Sens.*, *18*, 3145–3166, 1997.

Hall, F. G., K. F. Huemmrich, S. J. Goetz, P. J. Sellers, and J. E. Nickerson, Satellite remote sensing of surface energy balance: Success, failures, and unresolved issues in FIFE, *J. Geophys. Res.*, *97*, 19,061–19,089, 1992.

Jackson, T. J., D. M. Le Vine, A. Y. Hsu, A. Oldak, P. J. Starks, C. T. Swift, J. D. Isham, and M. Haken, Soil moisture mapping at regional scales using microwave radiometry: The Southern Great Plains hydrology experiment, *IEEE Trans. Geosci. Remote Sens.*, *37*, 2136–2151, 1999.

Jiang, L., and S. Islam, Estimation of surface evaporation map over southern Great Plains using remote sensing data, *Water Resour. Res.*, *37*, 329–340, 2001.

Koster, R., and M. Suarez, A comparative analysis of two land surface heterogeneity representations, *J. Clim.*, *5*, 1379–1390, 1992.

Kustas, W. P., and J. D. Albertson, Effects of surface temperature contrast on land-atmosphere exchange: A case study from Monsoon 90, *Water Resour. Res.*, *39*(6), 1159, doi:10.1029/2001WR001226, 2003.

Kustas, W. P., and J. M. Norman, Evaluation of soil and vegetation heat flux predictions using a simple two-source model with radiometric temperatures for partial canopy cover, *Agric. For. Meteorol.*, *94*, 13–25, 1999.

Kustas, W. P., and J. M. Norman, Evaluating the effects of subpixel heterogeneity on pixel average fluxes, *Remote Sens. Environ.*, *74*, 327–342, 2000.

Kustas, W. P., J. H. Prueger, K. S. Humes, and P. J. Starks, Estimation of surface heat fluxes at field scale using surface layer versus mixed layer atmospheric variables with radiometric temperature observations, *J. Appl. Meteorol.*, *38*, 224–238, 1999.

Kustas, W. P., T. J. Jackson, A. N. French, and J. I. MacPherson, Verification of patch- and regional-scale energy balance estimates derived from microwave and optical remote sensing during SGP97, *J. Hydrometeorol.*, *2*, 254–273, 2001.

Kustas, W. P., J. M. Norman, M. C. Anderson, and A. N. French, Estimating subpixel surface temperatures and energy fluxes from the vegetation index-radiometric temperature relationship, *Remote Sens. Environ.*, *85*, 429–440, 2003.

Mahrt, L., The bulk aerodynamic formulation over heterogeneous surfaces, *Boundary Layer Meteorol.*, *78*, 87–119, 1996.

Mahrt, L., Flux sampling errors for aircraft and towers, *J. Atmos. Oceanic Technol.*, *15*, 416–429, 1998.

Mason, P. J., The formation of areally-averaged roughness lengths, *Q.J.R. Meteorol. Soc.*, *114*, 399–420, 1988.

Massman, W., An analytical one-dimensional model of momentum transfer by vegetation of arbitrary structure, *Boundary Layer Meteorol.*, *83*, 407–421, 1997.

McNaughton, K. G., and T. W. Spriggs, A mixed-layer model for regional evaporation, *Boundary Layer Meteorol.*, *74*, 262–288, 1986.

Mecikalski, J. M., G. R. Diak, M. C. Anderson, and J. M. Norman, Estimating fluxes on continental scales using remotely-sensed data in an atmosphere-land exchange model, *J. Appl. Meteorol.*, *38*, 1352–1369, 1999.

Moran, M. S., Thermal infrared measurement as an indicator of plant ecosystem health, in *Thermal Remote Sensing in Land Surface Processes*, edited by D. A. Quattrochi and J. Luvall, Taylor and Francis, Philadelphia, Pa., in press, 2003.

Moran, M. S., T. R. Clarke, Y. Inoue, and A. Vidal, Estimating crop water deficit using the relation between surface-air temperature and spectral vegetation index, *Remote Sens. Environ.*, *49*, 246–263, 1994.

Moran, M. S., S. J. Maas, and P. J. Printer Jr., Combining remote sensing and modeling for estimating surface evaporation and biomass production, *Remote Sens. Rev.*, *12*, 335–353, 1995.

Moran, M. S., A. F. Rahman, J. C. Washburne, D. C. Goodrich, M. A. Weltz, and W. P. Kustas, Combining the Penman-Monteith equation with measurements of surface temperature and reflectance to estimate evaporation rates from semiarid grassland, *Agric. For. Meteorol.*, *80*, 87–109, 1996.

Moulin, S., A. Bondeau, and R. Delécolle, Combining agricultural crop models and satellite observations: From field to regional scales, *Int. J. Remote Sens.*, *19*, 1021–1036, 1998.

Norman, J. M., M. Divakarla, and N. S. Goel, Algorithms for extracting information from remote thermal-IR observations of the Earth's surface, *Remote Sens. Environ.*, *51*, 157–168, 1995a.

Norman, J. M., W. P. Kustas, and K. S. Humes, A two-source approach for estimating soil and vegetation energy fluxes from observations of directional radiometric surface temperature, *Agric. For. Meteorol.*, *77*, 263–293, 1995b.

Norman, J. M., W. P. Kustas, J. H. Prueger, and G. R. Diak, Surface flux estimation using radiometric temperature: A dual temperature difference method to minimize measurement error, *Water Resour. Res.*, *36*, 2263–2274, 2000.

Palluconi, F. D., and G. R. Meeks, Thermal infrared multispectral scanner (TIMS): An investigator's guide to TIMS data, Jet Propul. Lab., Calif. Inst. of Technol., Pasadena, Calif., 1985.

Price, J. C., The potential of remotely sensed thermal infrared data to infer surface soil moisture and evaporation, *Water Resour. Res.*, *16*, 787–795, 1980.

Price, J. C., Using spatial context in satellite data to infer regional scale evapotranspiration, *IEEE Trans. Geosci. Remote Sens.*, *GE-28*, 940–948, 1990.

Priestley, C. H. B., and R. J. Taylor, On the assessment of surface heat flux and evaporation using large-scale parameters, *Mon. Weather Rev.*, *100*, 81–92, 1972.

Raupach, M. R., and J. J. Finnigan, Scale issues in boundary-layer meteorology: Surface energy balances in heterogeneous terrain, *Hydrol. Processes*, *9*, 589–612, 1995.

Schuepp, P. H., M. Y. Leclerc, J. I. MacPherson, and R. L. Desjardins, Footprint prediction of scalar fluxes from analytical solutions of the diffusion equation, *Boundary Layer Meteorol.*, *50*, 355–373, 1990.

Seguin, B., J.-P. Lagouarde, and M. Saranc, The assessment of regional crop water conditions from meteorological satellite thermal infrared data, *Remote Sens. Environ.*, *35*, 141–148, 1991.

Shafer, M. A., C. A. Fiebrich, D. S. Arndt, S. E. Fredrickson, and T. W. Hughs, Quality assurance procedures in the Oklahoma mesonetwork, *J. Atmos. Oceanic Technol.*, *17*, 474–494, 2000.

Shuttleworth, W. J., and J. S. Wallace, Evaporation from sparse crops: An energy combination theory, *Q.J.R. Meteorol. Soc.*, *111*, 839–855, 1985.

Song, J., M. L. Wesely, M. A. LeMone, and R. L. Grossman, Estimating watershed evapotranspiration with PASS, part II, Moisture budgets during drydown periods, *J. Hydrometeorol.*, *1*, 462–473, 2000.

Sugita, M., and W. Brutsaert, Daily evaporation over a region from lower boundary layer profiles measured with radiosondes, *Water Resour. Res.*, *27*, 747–752, 1991.

Taconet, O., T. Carlson, R. Bernard, and D. Vidal-Madjar, Evaluation of a surface/vegetation parameterization using satellite measurements of surface temperature , *J. Clim. Appl. Meteorol.*, *25*, 1752–1767, 1986.

Twine, T. E., W. P. Kustas, J. M. Norman, D. R. Cook, P. R. Houser, T. P. Meyers, J. H. Prueger, P. J. Starks, and M. L. Wesely, Correcting eddy–covariance flux underestimates over a grassland, *Agric. For. Meteorol.*, *103*, 279–300, 2000.

Vidal, A., and C. Devaux-Ros, Evaluating forest fire hazard with a Landsat TM derived water stress index, *Agric. For. Meteorol.*, *77*, 207–224, 1995.

Wierenga, J., Roughness-dependent geographical interpolation of surface wind speed averages, *Q. J. R. Meteorol. Soc.*, *112*, 867–889, 1986.

Zhan, X., W. P. Kustas, and K. S. Humes, An intercomparison study on models of sensible heat flux over partial canopy surfaces with remotely sensed surface temperatures, *Remote Sens. Environ.*, *58*, 242–256, 1996.

M. C. Anderson and J. M. Norman, Department of Soil Science, University of Wisconsin, Madison, 1525 Observatory Drive, Madison, WI 53706, USA. (jmnorman@facstaff.wisc.edu)

G. R. Diak and J. Mecikalski, Space Science and Engineering Center, University of Wisconsin, Madison, Madison, WI 57306, USA.

A. N. French, Hydrological Sciences Branch, NASA Goddard Space Flight Center, Greenbelt, MD 20771, USA.

W. P. Kustas and T. J. Schmugge, Hydrology and Remote Sensing Laboratory, USDA-ARS, Building 007, BARC West, Beltsville, MD 20705, USA.

B. C. W. Tanner, 157 S. 100 W, Mendon, UT 84325, USA.

R. Torn, Department of Atmospheric Science, University of Washington, Seattle, WA 98195, USA.

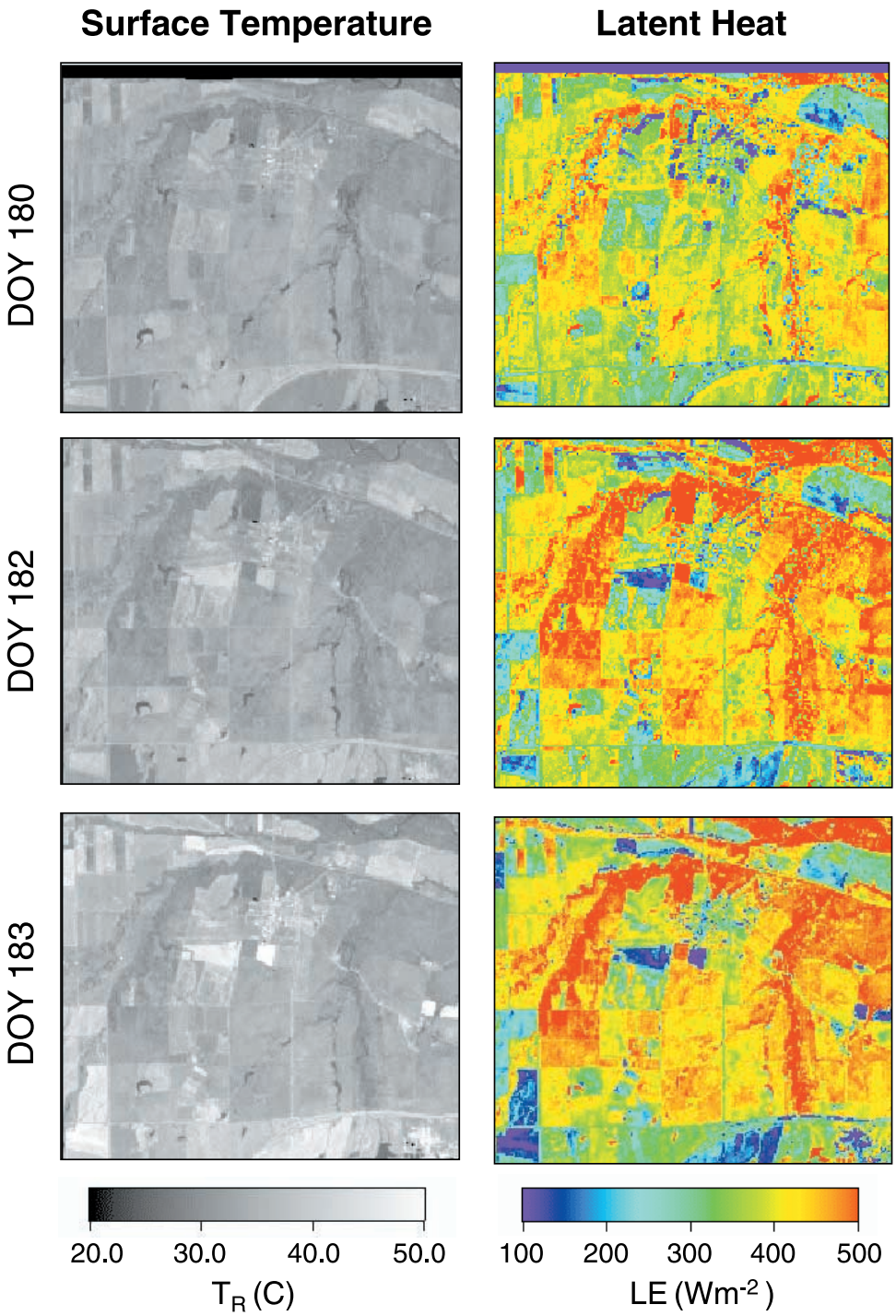

Figure 5. Maps at 24-m resolution of surface radiometric temperature (left) and disaggregated latent heat flux estimates (right) over the El Reno study area for DOY 180, 182, and 183.